-RESEARCH PAPER-

International Journal of Mining and Geo-Engineering

IJMGE

IJMGE 60-2 (2026) 113-122

DOI:10.22059/IJMGE.2025.401349.595298

Performance assessment of structured and unstructured meshes in inversion of electrical resistivity and induced polarization surveys: Kabudan gold area, NE Iran

Seyed Mohammad Sadatian Jouybari [a] , Ahmad Afshar [a, *] , and Hamideza Ramazi [a]

[a] *Faculty of Mining Engineering, Amirkabir University of Technology, Tehran, Iran.*

Article History:

Received: 15 August 2025.
Revised: 29 September 2025.
Accepted: 01 November 2025.

ABSTRACT

This research investigated the inversion of electrical resistivity and induced polarization (IP) data acquired along geoelectrical profiles in the Kabudan gold prospect, Razavi Khorasan Province, northeastern Iran. To achieve higher modeling accuracy, two discretization schemes—structured quadrilateral meshes and unstructured triangular meshes—were implemented. The inversion results from both approaches were generally consistent and successfully depicted major subsurface geological features; however, the triangular mesh configuration achieved a lower RMS error and more effectively resolved fine-scale structural variations. Interpretation of the results delineated several geophysical anomalies, some of which showed strong agreement with drilling and assay data, most notably in borehole BH02. While resistivity models displayed the highest correlation with drill-core information, chargeability models provided complementary constraints for resolving sulfide-rich zones. Overall, the integration of geoelectrical survey results with drilling data proved to be a reliable approach for the detection of sulfide mineralization zones and for enhancing the resolution of subsurface structural interpretations.

Keywords: *Electrical Resistivity; Chargeability; Inversion; Unstructured mesh; Structured mesh.*

1. Introduction

Geophysics, broadly defined, involves studying the Earth through measurements of variations in physical parameters associated with subsurface properties [1]. As non-invasive tools, geophysical methods are widely applied in engineering, environmental, and mineral exploration to characterize the subsurface efficiently in terms of cost and time[2, 3]. In mineral exploration, these methods exploit contrasts between host rocks and mineralized zones, playing a key role in identifying ore deposits [4]. The advantage of geophysical surveys lies in their ability to cover large areas rapidly and continuously, unlike point-based techniques such as drilling or trenches [5]. This enables the detection of geological anomalies and structures, even under complex terrains or thick overburden. When combined with advanced modeling and inversion frameworks, geophysical methods improve subsurface imaging and the accuracy of mineral targeting.

Gold exploration is economically important, but surface observations alone often fail to locate prospective zones. Surface geoelectrical methods, especially resistivity and induced polarization (IP) surveys, enhance detection of favorable zones for gold and base metals, improving targeting precision [6]. The main challenge is reliable integration of geophysical data with geological models, particularly in structurally complex or heterogeneous areas. Quantitative modeling and numerical algorithms are therefore critical for reducing interpretational uncertainty [7].

Among geophysical techniques, resistivity and IP are central to metallic ore exploration, especially for sulfide mineralization. Measured parameters such as resistivity and chargeability reflect rock properties including porosity, saturation, and mineral composition [8]. IP measures secondary electric fields induced in the subsurface, either in the time domain (decay voltage over time) or frequency domain (apparent resistivity at low frequencies) [9]. Advances now allow 3D and 4D applications, enabling spatiotemporal monitoring of resistivity variations for improved mapping [10].

Geophysical inversion reconstructs the spatial distribution of conductivity by comparing calculated responses from a model with field data, iteratively refining the model until agreement is achieved [8, 11]. Integrated inversion has proven effective in mineral exploration, as demonstrated at the Mt. Milligan Cu–Au deposit [12]. Inversion outputs provide reliable images of subsurface physical properties such as conductivity and chargeability, supporting identification of mineralized zones [13, 14].

The importance of combining geophysical and drilling data is evident for resource estimation and borehole optimization. Mostafaei and Ramazi (2019) showed that integrating resistivity and IP data with drilling can reduce borehole numbers by up to 30% while improving copper grade estimation. Forward modeling, using finite difference (FD) or finite element (FE) methods, predicts geophysical responses for a given subsurface scenario, forming the basis of inversion. FE methods handle unstructured meshes, making them suitable for 2D and 3D modeling in complex terrains, whereas FD methods are simpler but limited to structured grids [11, 15-17].

Previous studies focused mainly on meshing strategies in geotechnical or non-metallic contexts. This study evaluates structured

---

* Corresponding author. *E-mail address:* : a.afshar@aut.ac.ir (A. Afshar).

versus unstructured meshes in real-world gold exploration, comparing outputs from commercial Res2DInv and open-source ResIPy. Res2DInv uses smoothness-constrained least squares with structured meshes [18], while ResIPy supports both structured and unstructured meshes with Python API integration [19-22].

The Kabudan gold prospect in northeastern Iran, with complex geology, provides an ideal case to assess meshing strategies. This study inverts resistivity and IP datasets using ResIPy with both mesh types and compares results to Res2DInv models, validated against exploratory borehole data. This allows evaluation of inversion performance, geological plausibility, and targeting accuracy.

2. Geological setting

The Kabudan mineralization complex is located north of Bardaskan, within the Taknar structural zone of northeastern Iran. According to the tectonic subdivision of Iran, the Taknar zone is part of the Central Iranian structural domain [23, 24]. Geotechnically, the Taknar zone occupies an intermediate position between the Lut Block to the south and the Sabzevar zone to the north, and is bounded by the Doruneh (Great Kavir) Fault to the south and the Taknar (Rivash) Fault to the north [25, 26].

The Taknar Formation comprises mica schist units, dacitic–rhyolitic volcanic rocks, and a suite of intrusive bodies ranging from granite–granodiorite to metadiabase and meta gabbro–diorite [27]. These units represent part of the uplifted Precambrian to Paleozoic basement of Central Iran, overlain by Mesozoic–Cenozoic volcanic–sedimentary sequences. From a mineral potential perspective, the zone is noteworthy for its metallic resources—gold, copper, lead, zinc, silver, and iron—as well as important non metallic commodities such as feldspar, bauxite, building materials, and industrial clays [28].

Metallic mineralization in the Bardaskan area, particularly gold, occurs mainly as epithermal and disseminated types [29]. The dominant hydrothermal alterations are chloritization, sericitization, and silicification. The principal ore minerals are pyrite, chalcopyrite, and native gold, which are concentrated primarily within siliceous veins and sericitically altered zones [30]. Several other epithermal gold prospects and deposits—such as Sebandoon, Bijourd, and Damanghor—are identified in the northern part of the Kabudan area [31, 32].

The study area lies immediately north of Kabudan village, approximately 15 km north of Bardaskan, in Razavi Khorasan Province. Two principal alteration types are present: silicic and iron oxide alteration. Silicic alteration is expressed as pervasive replacement of host rocks by silica, mostly along fractures and vein margins, affecting rhyolitic volcanics and sericitic schists. Iron oxide alteration is more widespread and is commonly associated with fault structures or occurs adjacent to diabase dikes; it is characterized by hematite and limonite, producing distinctive red and yellow coloration. The geological map of the area is shown in Figure 1.

3. Materials and Methods

Given the absence of mineral outcrops in the Kabudan gold prospect, six rectangular arrays with a total electrode spread of AB = 600 m were deployed to delineate potential anomalies and provide a basis for more detailed follow up investigations. Subsequently, to examine the vertical extent of mineralization and monitor the depth continuity of anomalies identified in the rectangular array chargeability and resistivity maps, four geoelectrical profiles were designed and surveyed. Figure 2 illustrates the field survey operations and the geophysical equipment utilized during the data acquisition.

The surveys comprised both electrical resistivity and IP measurements, the results of which confirmed the presence and persistence of anomalous zones at greater depths. The employed electrode configurations included pole–dipole and dipole–dipole arrays, with their acquisition parameters summarized in Table 1. Figure 3 illustrates the anomaly patterns obtained from modeling the rectangular array chargeability and resistivity datasets, together with the locations of the surveyed profiles and exploratory boreholes.

To maintain focus and avoid excessive figures, and given the limited availability of drilling data, only two profiles—P01 and P02—were selected for detailed analysis in this paper.

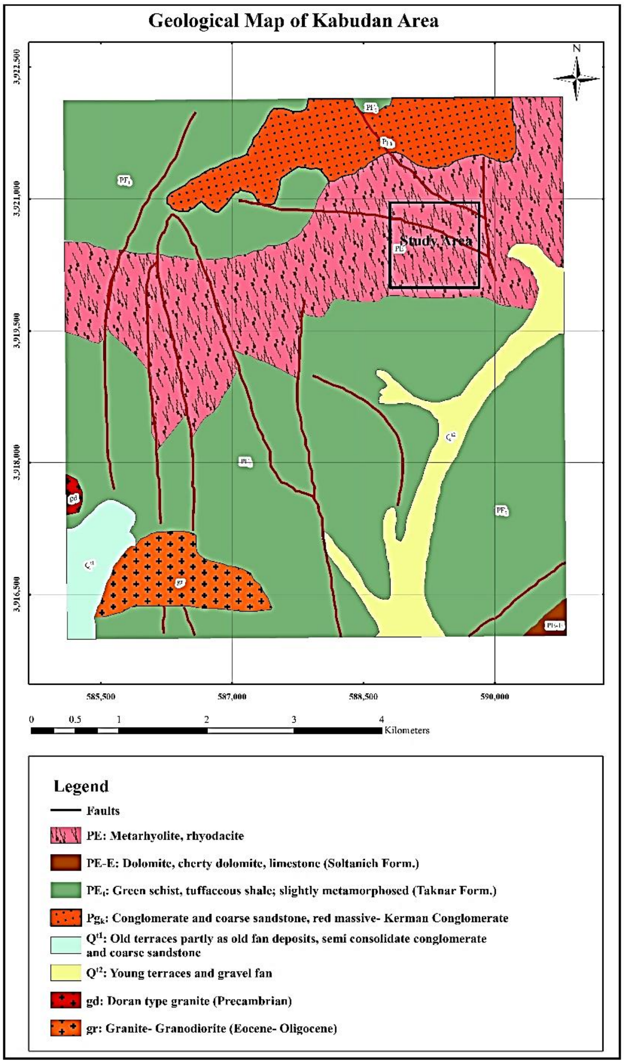

Figure 1. Geological map of the Kabudan area, north of Bardeskan, extracted from the 1:100,000 Bardeskan geological map.

The acquired datasets, after preliminary processing, were inverted to produce two-dimensional resistivity and chargeability sections. Inversion serves as a powerful tool for recovering the spatial distribution of subsurface physical properties from measured data, thereby enabling quantitative interpretation of geological structures [33]. In this process, the subsurface is represented as a mathematical model consisting of a set of parameters that describe the geometric and physical characteristics of the medium. The underlying principle of inversion is to assess the degree of fit between the response of the numerical model and the observed data, mathematically expressed by an objective function that quantifies the misfit between calculated and measured values as a function of the model parameters [1].

It is important to note that the goal of geophysical inversion is not to produce an exact reconstruction of the true subsurface, but rather to derive a model that best fits the observed data within predefined constraints [33]. One of the most widely applied statistical techniques for optimizing this fit is the least squares method, first introduced by Carl Friedrich Gauss in 1794. In this approach, the optimal solution minimizes the sum of the squared differences between the observed and calculated data, known as the sum of squared errors [34].

In the RES2DINV software, the subsurface environment is discretized into a grid of rectangular cells, with the model parameters corresponding to the resistivity values of these cells. The input data consist of measured apparent resistivity values, while the forward responses of two-dimensional models are computed using the finite element method [35]. The dimensions of the model cells are automatically adjusted by the program according to the spatial distribution of the data points [36]. The inversion task thus becomes one of finding resistivity values that minimize the discrepancy between measured and calculated apparent resistivities [37].

The inversion algorithm implemented in RES2DINV is based on the smoothness constrained least squares method [38]. The discrepancy between the calculated and the measured (observed) data is quantified using the root mean square (RMS) error criterion [36]. The smoothness constrained Gauss–Newton procedure is among the most widely adopted approaches for two and three-dimensional inversion of apparent resistivity datasets.

Figure 2. Field survey operations and the geophysical equipment utilized during the data acquisition.

Table 1. Specifications of the acquired profiles over the observed chargeability anomalies of the Rectangle array.

Profile Name	Length (m)	Array	Electrode Spacing
P1	500	Dipole-Dipole	20
P2	500	Pole-Dipole	20
P3	500	Pole-Dipole	20
P4	300	Pole-Dipole	10

The R2 code is designed for forward modeling and inversion of two- and three-dimensional electrical current flow in either triangular or quadrilateral element meshes. In forward modeling, transfer resistances or apparent resistivities are computed for a given set of four electrode measurements and a specified resistivity distribution. These computations may be carried out explicitly in forward mode or implicitly during inversion. The governing equations are solved using the finite element method (FEM) in which the model domain is discretized into a mesh of three node triangular or four node quadrilateral elements, and electric potentials are calculated at the element nodes [39].

Although quadrilateral meshes are simpler to construct, they typically provide lower computational efficiency compared to triangular elements. The inversion process in R2 is iterative, aiming to minimize an objective function that incorporates both the data misfit and the model roughness. A Gauss–Newton optimization scheme is used to solve the system. In this framework, model parameters are expressed logarithmically in terms of electrical conductivity, while the data can be processed either as resistivity values or as their logarithms [39].

The cR2 code was developed for complex resistivity (CR) or induced polarization (IP) imaging using arbitrary electrode configurations. It is capable of performing both forward modeling and two-dimensional inversion on triangular or quadrilateral finite element meshes. The inversion procedure is based on a regularized objective function and a weighted least squares method [40]. In cR2, complex resistivity is defined in terms of magnitude and phase angle; in addition, the real and imaginary components of conductivity are computed, which are particularly important for analyzing subsurface conductivity and polarization behavior. Magnitude is always treated as positive, and a negative phase angle is interpreted as an equivalent positive induced polarization effect [41, 42].

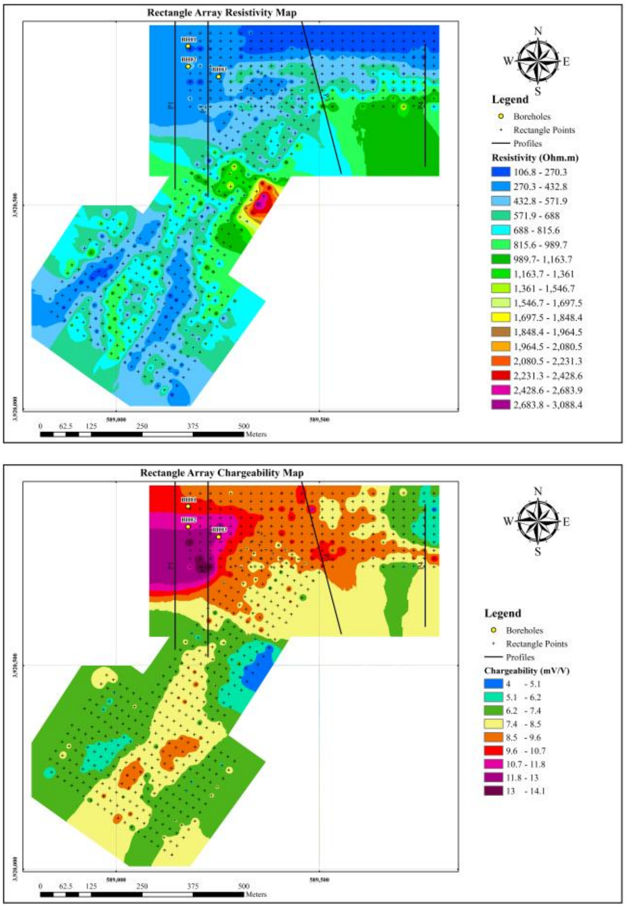

Figure 3. Electrical resistivity and chargeability maps obtained from the rectangular array.

Within the ResIPy software, two types of two-dimensional finite element meshes can be utilized: a structured quadrilateral mesh, and an unstructured triangular mesh. For forward modeling, the R2 inversion engine computes nodal voltages under the assumption of a dipole current source; consequently, electrode positions must align precisely with mesh nodes. The accuracy of the voltage field solution is strongly dependent on mesh discretization density and the proximity of nodes to electrode positions, since voltage gradients are steepest in those regions. Mesh designs therefore incorporate a refined element zone around the electrodes, embedded within a coarser, larger mesh extending laterally and vertically, to allow for non-flux (Neumann) boundary conditions that simulate an infinite domain—reflecting the fact that the injected current propagates beyond the immediate survey area [43].

In ResIPy, quadrilateral meshes are defined as an array of X and Z coordinates forming a structured grid. They typically consist of a central fine mesh region aligned with the survey geometry and surrounded by a coarser peripheral region. By contrast, triangular meshes offer greater flexibility, making them suitable for more complex survey geometries. In both mesh types, refinement around each electrode can be specified—smaller refinement lengths produce finer meshes, but overly fine elements in low sensitivity regions should be avoided to prevent unnecessary computation. Overall, quadrilateral meshes require less generation time, whereas triangular meshes provide enhanced adaptability and tend to yield superior performance in areas with rugged or complex topography [43].

4. Results and discussion

Following the acquisition of the geoelectrical profiles, the datasets were pre processed and subsequently inverted. Given the necessity of validating the inversion derived sections, the limited availability of drilling data—restricted to areas adjacent to Profiles P01 and P02—and the aim of minimizing redundant figures, only these two profiles were examined in detail.

The first step in the ResIPy inversion workflow involved generating and refining the computational meshes. Figure 4 illustrates the structured quadrilateral and unstructured triangular meshes created for both the resistivity and chargeability datasets of Profiles P01 and P02.

For inversion, both structured quadrilateral and unstructured triangular meshes were tested using the ResIPy platform, alongside the widely used commercial software RES2DInv. Once the meshes were generated, inversion was performed, and the resulting models were rendered for each profile. The RMS errors achieved for the resistivity and chargeability inversions of each profile are summarized in Table 2. Also, Figure 5 shows the variation of RMS error iterations for rectangular and triangular meshes of profiles P01 and P02.

Figure 6 presents the observed and calculated data sections for Profile P01 using triangular and quadrilateral meshes within ResIPy.

Profile P01, a 500 m north–south line acquired with a dipole–dipole array, revealed two distinct conductive zones at 140–200 m and 340–400 m. It should be mentioned that between the profile start and 140 m, rhyolitic units and acidic tuffs were encountered, displaying higher resistivity values than the surrounding formations. Chargeability data indicate that the first zone has high chargeability values, confirming the likely presence of sulfide mineralization. In contrast, the second zone exhibits low chargeability, suggesting shale or similar lithologies. Figure 7 compares the inversion results for P01 from both ResIPy and RES2DInv.

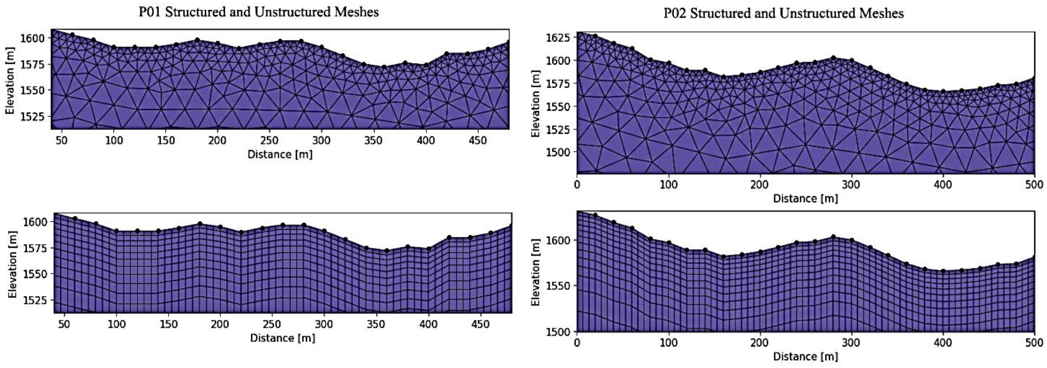

Figure 4. Structured and unstructured meshes generated for profile inversion modeling.

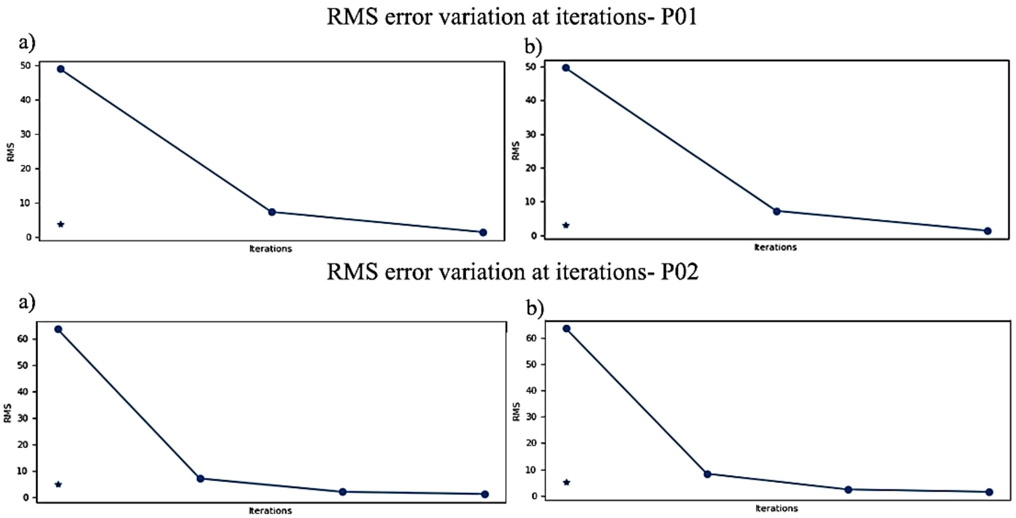

Figure 5. variation of RMS error iterations for rectangular and triangular meshes of profiles P01 and P02. a) for triangular mesh, b) for rectangular mesh.

Table 2. RMS error of the inversion process performed with structured and unstructured meshes.

Profile	RMS misfit			
	Triangular Mesh		Quadrilateral Mesh	
	Resistivity	Chargeability	Resistivity	Chargeability
P01	1	0.462	1	0.498
P02	1.13	0.380	1.18	0.540

Profile P02, collected with a pole–dipole configuration over 500 m, displayed a conductive, high-chargeability anomaly between 180–220 m, indicative of sulfide mineralization, The observed and calculated data sections for P02, produced using ResIPy with both mesh types, are shown in Figure 8. From the profile start to approximately 180 m, rhyolite and metarhyolite units dominate—clearly imaged in the resistivity section. Around 180 m, a distinct discontinuity appears in all three inversion sections.

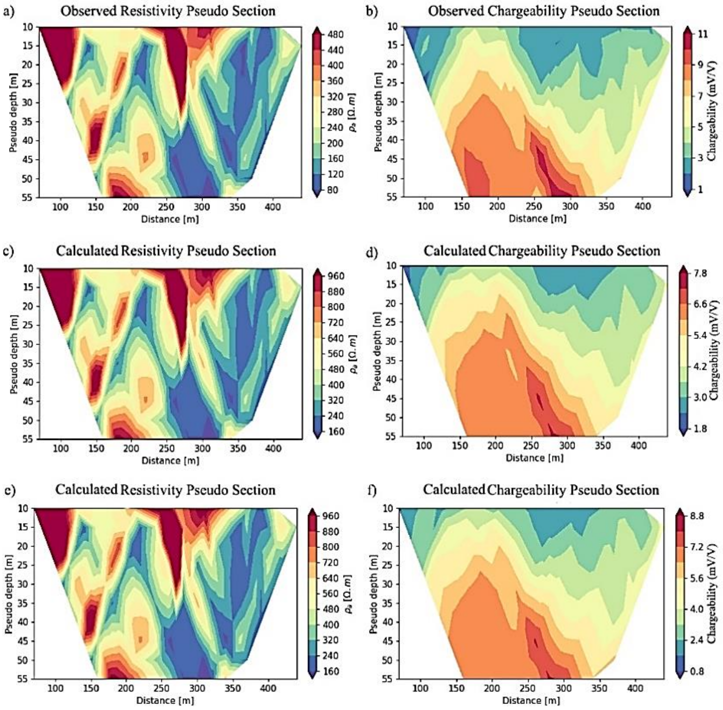

Figure 6. Observed and calculated sections of profile P01 using ResIPy: a-b) observed data, c-d) calculated data with structured quadrilateral mesh, e-f) calculated data with unstructured.

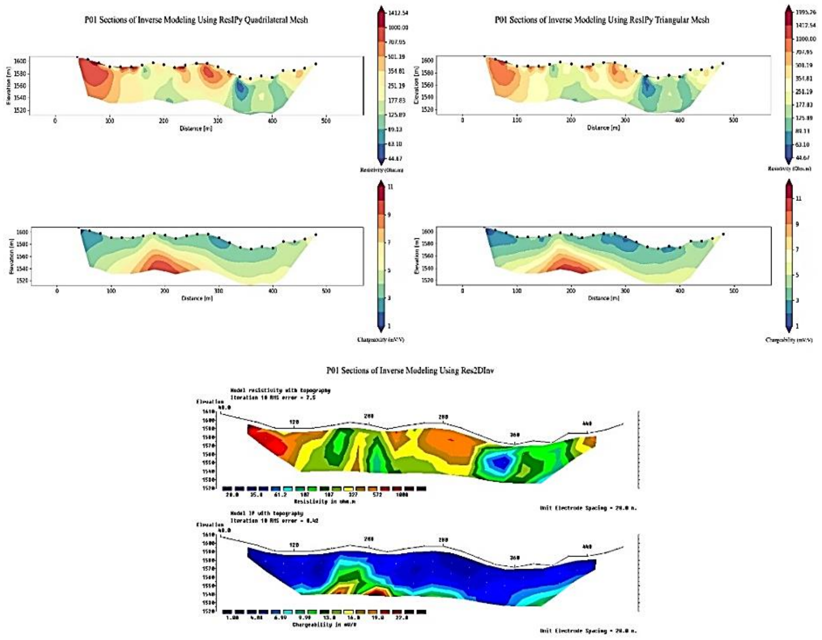

Figure 7. Comparison of inverted models for profile P01 obtained using structured and unstructured meshes in ResIPy and the commercial software RES2DInv: a-b) ResIPy quadrilateral mesh c-d) ResIPy triangular mesh, e-f) RES2DInv inversion results.

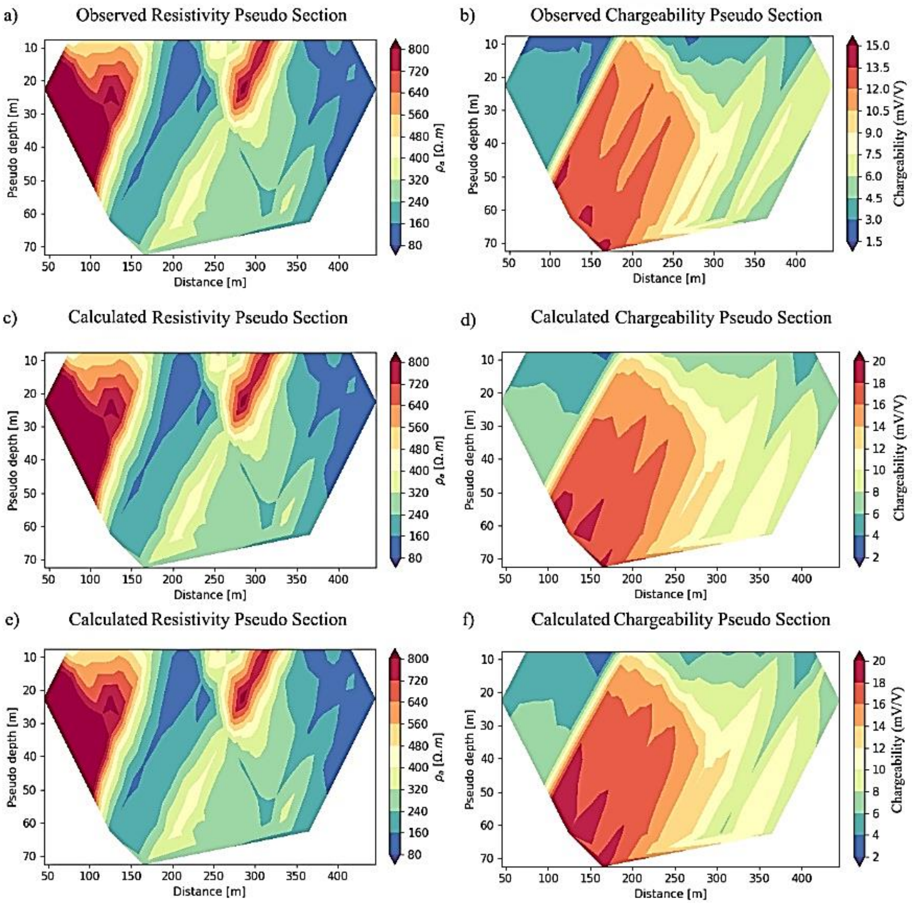

Figure 8. Observed and calculated sections of profile P02 using ResIPy: a-b) observed data, c-d) calculated data with structured quadrilateral mesh, e-f) calculated data with unstructured triangular mesh.

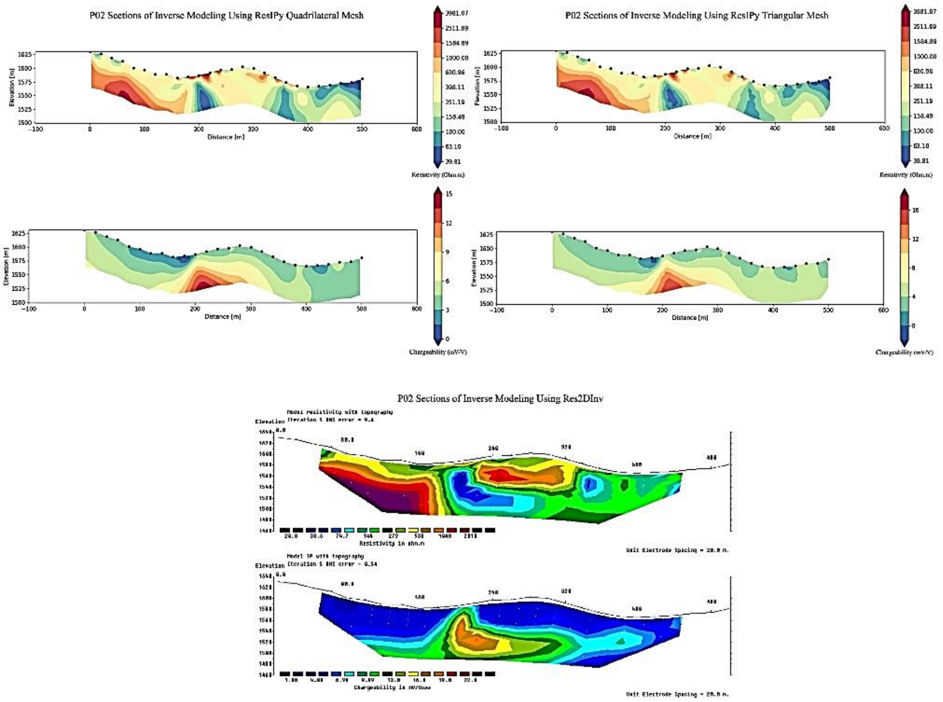

Figure 9. Comparison of inverted models for profile P02 obtained using structured and unstructured meshes in ResIPy and the commercial software RES2DInv: a-b) ResIPy quadrilateral mesh, c-d) ResIPy triangular mesh, e-f) RES2DInv inversion results.

From 240–340 m, high resistivity units devoid of significant chargeability anomalies are observed. Near the profile end, between 340–360 m, a deep conductive zone with moderate to high chargeability was detected. The inversion results from both platforms for P02 are compared in Figure 9.

A conductive zone with elevated suggests the presence of sulfide mineralization. This interpretation is strongly supported by borehole BH02 where pyrite and chalcopyrite were encountered at similar depths. Comparable correlations between high chargeability anomalies and sulfide-bearing zones have been reported in several related studies (e.g. Mostafaei and Ramazi, 2019) [44]. This strengthens the reliability of the inversion models for guiding drilling in analogous exploration settings.

Chargeability anomalies in the study area do not exhibit a direct correlation with gold grade (Au) and are primarily associated with sulfide-bearing zones containing pyrite and chalcopyrite, occasionally accompanied by magnetite. Given that gold occurrences are confined to these sulfide zones, high chargeability can serve as a reliable indicator of sulfide presence and a key guide for gold mineralization exploration.

Figure 10, illustrates the variation of gold grades at different depths of the borehole, ranging from 50 m to 97 m. As shown, the highest gold grades are observed within sections of the borehole corresponding to sulfide-bearing zones.

Figure 11 presents the relationship between chargeability and gold grade, indicating that high chargeability values do not directly correspond to high gold grades. Nevertheless, elevated gold grades are generally associated with chargeability values exceeding 10 mV/V, predominantly occurring within sulfide-bearing zones.

This analysis underscores the utility of high chargeability as a geophysical proxy for delineating sulfide-bearing zones and guiding gold exploration, even when a direct one-to-one correlation with gold grade is absent. ResIPy also supports quasi 3D modeling through the simultaneous inversion of multiple parallel 2D profiles. In this approach, several 2D lines are meshed together within a 3D space based on the true electrode coordinates, and a joint inversion is executed. Figure 12 displays the 3D resistivity models for Profiles P01 and P02 obtained using both structured and unstructured meshes.

Three exploratory boreholes were drilled within the study area at the locations shown in Figure 13, on the anomaly map derived from the rectangular array dataset. Their specifications are listed in Table 3. A three-dimensional model of these boreholes, together with their assay data, is presented in Figure 13. Comparison of the borehole results with the inverted geoelectrical sections demonstrated that all three sections successfully depicted the anomalies and the general distribution of lithological units.

The borehole data confirmed the overall consistency and geological plausibility of the geophysical models, indicating close agreement between inversion derived structures and the actual subsurface conditions.

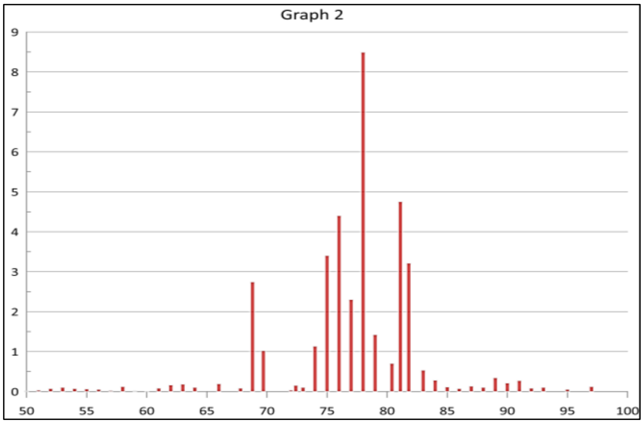

Figure 10. Variation of gold grades at different depths of the borehole, ranging from 50 m to 97m.

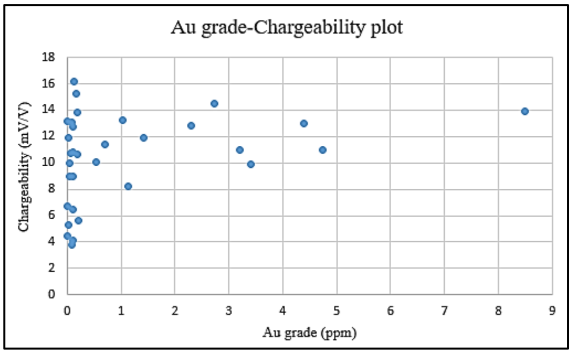

Figure 11. Scatter distribution diagram of chargeability data against gold grade.

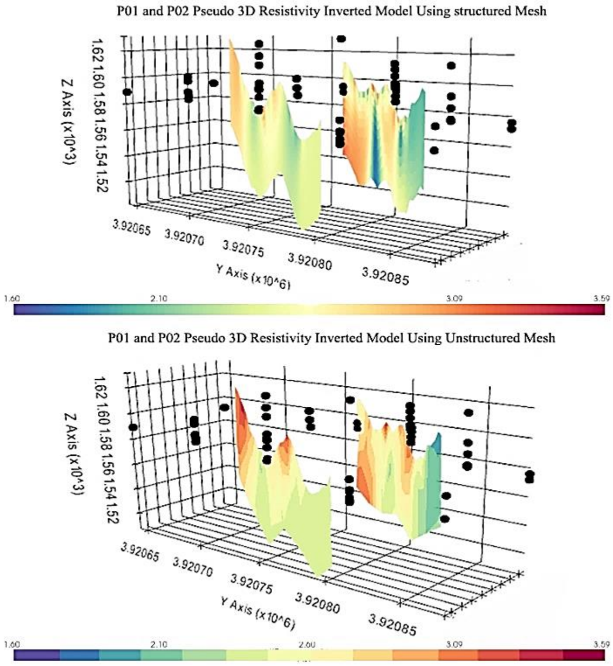

Figure 12. Sections resulting from the inversion modeling of resistivity data for profiles P01 and P02, using structured and unstructured meshes in ResIPy.

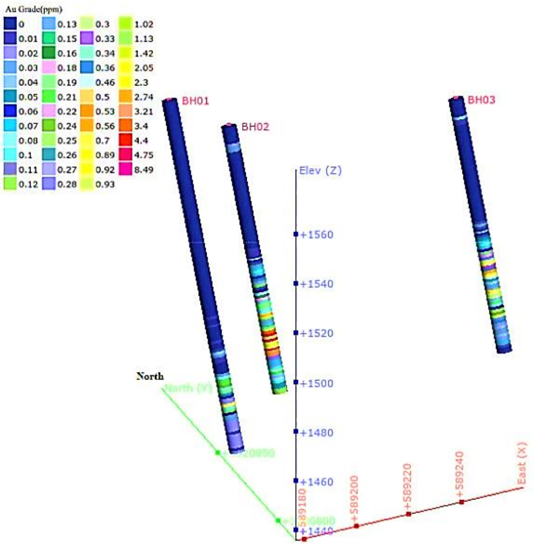

Figure 13. Three-dimensional model of the drilled boreholes with their corresponding assay results, viewed from the southwest.

Table 3. Specifications of the boreholes drilled in the Kabudan area.

Borehole Name	X	Y	Dip	Depth (m)	Az (°)
BH01	589177	3920891	70	130	172
BH02	589177	3920841	70	101	172
BH03	589282	3920816	70	109	172

The lithologies encountered in BH02 which coincides with the high chargeability anomaly identified along profile P02, consist of pyrite, metamorphosed sandstone, and green schist from depths of 68 m to approximately 75 m. The highest recorded gold grade in this borehole—8 ppm—was measured at 77–78 m depth. Overall, the high grade interval in BH02 extends from 75 m to 83 m, averaging 5–8 ppm Au, and comprises magnetite, pyrite, chalcopyrite, and green schist. Below 83 m, both gold content and lithological character change, marking the downward termination of the anomaly. The resistivity models exhibit strong correlation with the drilling data. The chargeability model produced by ResIPy, while successfully outlining the general anomaly, mapped a spatial extent slightly larger than that observed in the boreholes. Similarly, the Res2DInv chargeability inversion depicted an anomaly that extends marginally deeper than the true geological boundaries. Nevertheless, both chargeability models effectively delineated the main target zones.

For apparent resistivity, the sections generated from both mesh types (structured quadrilateral and unstructured triangular) showed substantial overlap and mutual confirmation. However, the unstructured triangular mesh model provided a more precise representation of subsurface heterogeneities and captured finer scale structural details. This improved resolution was also reflected in a lower RMS error, underscoring the superiority of the triangular mesh in reproducing the true geological features of the area.

The highest gold grade recorded in BH03—drilled on the eastern segment of profile P02—was 2 ppm, hosted within sericite schist and silicified zones. BH01, located 50 m north of BH02, yielded negligible gold grades. In general, the inversion models showed strong agreement with the empirical drilling data. All geoelectrical modeling approaches successfully revealed a concealed anomaly within the prospect area, and ResIPy, as an open source non-commercial platform, demonstrated high capability in imaging this anomaly. Only minor variations were noted in the chargeability models. Figure 14 presents the three-dimensional borehole model alongside the chargeability sections of profiles P01 and P02, illustrating their spatial correspondence.

It should be noted that the interpretations presented here are based solely on the dataset acquired within this specific exploration block and reflect the geological and geophysical characteristics of this localized area; therefore, they should not be generalized as a universal conclusion.

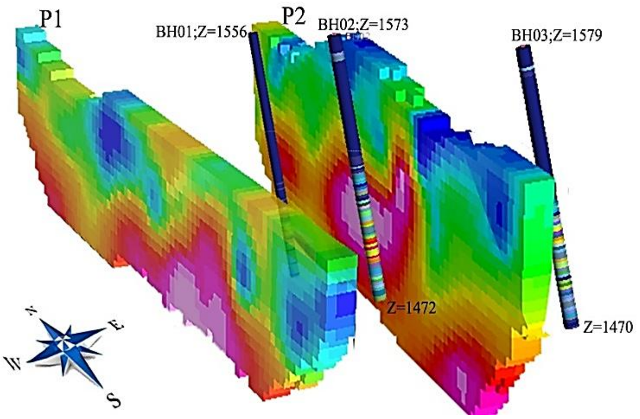

Figure 14. Three-dimensional visualization of borehole locations in relation to the chargeability inversion sections for Profiles P1 and P2.

5. Conclusions

The inversion results obtained from electrical resistivity and chargeability surveys in the Kabudan gold prospect exhibit a remarkable correspondence with both geological evidence and borehole drilling data. Analysis of the geoelectrical datasets (resistivity and chargeability) using ResIPy and RES2DInv clearly demonstrated that mesh configuration exerts a direct and significant influence on inversion quality and accuracy. Inversion sections generated from structured quadrilateral and unstructured triangular meshes showed strong overall consistency and mutual confirmation; however, the triangular unstructured mesh models provided superior capability in representing and resolving finer scale structural details and were characterized by lower RMS errors. This finding underscores the critical role that flexible mesh designs can play in improving inversion quality and enhancing interpretational accuracy.

Validation of the inversion sections against data from the three available boreholes revealed excellent agreement between the geophysical results and the geological reality of the area. Along Profile P01, two conductive zones were identified—chargeability data indicated that one corresponds to metal sulfide mineralization, while the other is likely associated with shale units. On Profile P02, conductive and chargeable zones coinciding with structural discontinuities were clearly delineated. The correspondence between these anomalies and the drilling records, particularly in borehole BH02, attests to the reliability of the inversion results and the effectiveness of the applied methodologies.

A comparative analysis of resistivity and chargeability models further revealed that although both successfully delineated the anomalies, resistivity models showed a higher degree of concordance with drilling results. ResIPy, as an open source and non commercial platform, proved especially effective in imaging concealed anomalies. Nevertheless, it should be emphasized that these findings are specific to the Kabudan prospect area and may not be directly generalized to other geological settings. This limitation does not diminish the scientific value of the current work; rather, it highlights the importance of conducting similar studies on a wider scale.

In conclusion, this investigation confirms that geoelectrical methods—particularly when integrated with drilling data—represent a powerful approach for detecting metallic mineralization and imaging subsurface heterogeneities. Furthermore, the demonstrated advantage of unstructured triangular meshes suggests a promising pathway for future inversion studies in geologically complex terrains and under diverse survey conditions

Acknowledgement

The authors would like to express their sincere gratitude to the Faculty of Mining Engineering at Amirkabir University of Technology for providing essential research facilities and a supportive academic environment throughout this study. The authors also wish to thank Komeh Ma'dan Pars Co. for generously providing access to exploratory data, which greatly contributed to the advancement of this research.

References

[1]. Dentith, M., & Mudge, S. T.; "Geophysics for the mineral exploration geoscientist", Cambridge University Press, 2014.

[2]. Lenhare, B.D., Moreira, C.A., & Ilha, L.M.; "Gold ore identification in Santa Catarina Gabbro using electrical resistivity tomography (ERT) and visualization of mineralization in three dimensions, São Sepé, Rio Grande do Sul, Brazil", Geofísica internacional, 62(4): p. 591-606, 2023.

[3]. Deo, R. N., & Kodikara, J.; "Direct current resistivity and time domain induced polarization methods in soil corrosivity assessment for buried infrastructure", Journal of Applied

Geophysics, vol. 209, p. 104921, 2023.

[4]. Kearey, P., Brooks, M., & Hill, I.; "An introduction to geophysical exploration", John Wiley & Sons, 2002.

[5]. Mita, M., Glazer, M., Kaczmarzyk, R., Dąbrowski, M., & Mita, K.; "Case study of electrical resistivity tomography measurements used in landslides investigation, Southern Poland", Contemporary Trends in Geoscience, vol. 7, no. 1, pp. 110-126, 2018.

[6]. Oldenburg, D. W., & Li, Y.; "Inversion for applied geophysics: A tutorial", 2005.

[7]. Groves, D., & Foster, R.; "Archaean lode gold deposits, in Gold metallogeny and exploration", Springer, p. 63-103, 1991.

[8]. Power, C., Tsourlos, P., Ramasamy, M., Nivorlis, A., & Mkandawire, M.; "Combined DC resistivity and induced polarization (DC-IP) for mapping the internal composition of a mine waste rock pile in Nova Scotia, Canada", Journal of Applied Geophysics, vol. 150, pp. 40-51, 2018.

[9]. Dahlin, T., Leroux, V., & Nissen, J.; "Measuring techniques in induced polarisation imaging", Journal of Applied Geophysics, 50(3): p. 279-298, 2002.

[10]. Loke, M. H., Chambers, J. E., Rucker, D. F., Kuras, O., & Wilkinson, P. B.; "Recent developments in the direct-current geoelectrical imaging method", Journal of applied geophysics, 95: p. 135-156, 2013.

[11]. Rücker, C.; "Advanced electrical resistivity modelling and inversion using unstructured discretization", Universität Leipzig, PhD Thesis, 2011.

[12]. Oldenburg, D.W., Li, Y., & Ellis, R.G.; "Inversion of geophysical data over a copper gold porphyry deposit: A case history for Mt. Milligan", Geophysics, 62(5): p. 1419-1431, 1997.

[13]. Loke, M. H.; "Tutorial: 2-D and 3-D Electrical Imaging Surveys", Geotomo Software, Malaysia, 2011.

[14]. Bala, G. A., Bery, A. A., Gnapragasan, J., & Akingboye, A. S.; "Development of novel resistivity-chargeability statistical relationships for subsurface characterization at Langkawi, Kedah", Environmental Science and Pollution Research, pp. 1-13, 2024.

[15]. Erdoğan, E., Demirci, I., & Candansayar, M. E.; "Incorporating topography into 2D resistivity modeling using finite-element and finite-difference approaches", Geophysics, vol. 73, no. 3, pp. F135-F142, 2008.

[16]. Akça, I., & Basokur, A. T.; "Extraction of structure-based geoelectric models by hybrid genetic algorithms", Geophysics, vol. 75, no. 1, pp. F15-F22, 2010.

[17]. Demirci, I., Erdoğan, E., & Candansayar, M.E.; "Two-dimensional inversion of direct current resistivity data incorporating topography by using finite difference techniques with triangle cells: Investigation of Kera fault zone in western Crete", Geophysics, 77(1): p. E67-E75, 2012.

[18]. Abedi, M.; "A focused and constrained 2D inversion of potential field geophysical data through Delaunay triangulation, a case study for iron-bearing targeting at the Shavaz deposit in Iran", Physics of the Earth and Planetary Interiors, vol. 309, p. 106604, 2020.

[19]. Samouëlian, A., Cousin, I., Richard, G., Tabbagh, A., & Bruand, A.; "Electrical resistivity imaging for detecting soil cracking at the centimetric scale", Soil Science Society of America Journal, 67(5): p. 1319-1326, 2003.

[20]. Biabani, A., Abedi, M., Norouzi, G.H., & Mojarab, M.; "Forward and inverse modeling of electrical resistivity geophysical data of a landslide surface discretized by unstructured mesh - A case study: Tehran-North Freeway", Journal of Radar Applications and Geoscience, vol. 8, no. 3, pp. 202-212, doi: 10.22044/jrag.2023.12148.1339, 2024.

[21]. Damavandi, K., Abedi, M., Norouzi, G.H., & Mojarab, M.; "Geoelectrical modelling of a landslide surface through an unstructured mesh", Bulletin of Geophysics & Oceanography (BGO), vol. 63, no. 2, 2022.

[22]. Mohammadi, A., Abedi, M., MirMohammadi, M. S., & Zarean, A.; "Electrical imaging of gold-bearing mineralization zones through 3D geophysical modeling", International Journal of Mining and Geo-Engineering, 2025.

[23]. Stöcklin, J.; "Structural history and tectonics of Iran: a review", AAPG Bulletin, vol. 52, no. 7, pp. 1229-1258, 1968.

[24]. Berberian, M., & King, G.; "Towards a paleogeography and tectonic evolution of Iran", Canadian Journal of Earth Sciences, vol. 18, no. 2, pp. 210-265, 1981.

[25]. Lindenberg, H. G., Corler, K., & Ibbeken, H.; "Stratigraphy, Structure and orogenetic evolution of Sabzevar zone in the area of Oryan Khorasan, NE Iran", GSI Report 51, Tehran, 1982.

[26]. Muller, R., & Walter, R.; "Geology of the Precambrian-Paleozoic Taknar Inlier northwest of Kashmar, Khorasan Province northeast Iran", 1983.

[27]. Ghasemi Siani, M., Mehrabi, B., & Gholizadeh, K.; "Geology, mineralogy and geochemistry of Kabudan Fe-rich volcanogenic ore mineralization, north of Bardaskan, Taknar zone," Earth science research (in Persian), pp. 253-272 , doi: 10.52547/esrj.10.4.253, 2020.

[28]. Azmi, H., Moarefvand, P., & Maghsoudi, A.; "Resource estimation of the Damanghor gold deposit, based on geology and grade continuity", Geopersia, vol. 10, no. 2, pp. 381-394, 2020.

[29]. Hashemi, M., & Afzal, P.; "Identification of geochemical anomalies by using of number–size (N–S) fractal model in Bardaskan area, NE Iran", Arabian Journal of Geosciences, vol. 6, pp. 4785-4794, 2013.

[30]. Hashemi, M., Afzal, P., Rasa, I., Noghreian, M., KhosroTehrani, K., & Vothoughi Abedini, M.; "Geochemical anomaly separation by concentration-area fractal model in Bardaskan area, NE Iran", Journal of Mining and Metallurgy, vol. 46, pp. 1-10, 2010.

[31]. Hamami Pour, B., Tajeddin, H., & Barahmand, L.; "Geology and geochemistry of Sebandoon gold mine, north of Bardaskan: Example of epithermal gold mineralization in Ophiolitic host rocks", Conference: 18th Symposium of the Geological Society of Iran, 2014.

[32]. Abbasnia, H., Karimpour, M., & Malekzadeh Shafaroudi, A.; "Damanghor intermediate sulfidation epithermal Au mineralization, Northern Bardaskan: geology, alteration, mineralization, and geochemistry", Iranian Journal of Crystallography and Mineralogy, vol. 27, no. 3, pp. 621-634, 2019.

[33]. Oldenburg, D. W., Heagy, L., Haber, E., Cowan, D., & Shekhtman, R.; "Fundamentals of Inversion", University of British Columbia, 2015.

[34]. Menke, W.; "Discrete Inverse Theory", Geophysical Data Analysis, vol. 289, 1989.

[35]. Loke, M. H.; "Tutorial: 2-D and 3-D electrical imaging surveys", 2004.

[36]. RES2DINV ver. 3.59 for Windows XP/Vista/7, Geoelectrical Imaging 2D & 3DGEOTOMO SOFTWARE, Geotomo Software, Malaysia, 2010.

[37]. Loke, M.H., & Dahlin, T.; "A comparison of the Gauss–Newton and quasi-Newton methods in resistivity imaging inversion. Journal of applied geophysics", 49(3): p. 149-162, 2002.

[38]. deGroot-Hedlin, C., & Constable, S.; "Occam's inversion to generate smooth, two-dimensional models from magnetotelluric data", Geophysics, 55(12): p. 1613-1624, 1990.

[39]. Binley, A., & Slater, L.; "Resistivity and induced polarization: Theory and applications to the near-surface earth", Cambridge University Press, 2020.

[40]. Binley, A., & Kemna, A.; "DC resistivity and induced polarization methods, in Hydrogeophysics", Springer. p. 12 156-9, 2005.

[41]. Kemna, A., Räkers, E. & Binley, A.; "Application of complex resistivity tomography to field data from a kerosene-contaminated site", 3rd EEGS Meeting, European Association of Geoscientists & Engineers, pp. cp-95-00039, 1997.

[42]. Mwakanyamale, K., Slater, L., Binley, A., & Ntarlagiannis, D.; "Lithologic imaging using complex conductivity: Lessons learned from the Hanford 300 Area", Geophysics, vol. 77, no. 6, pp. E397-E409, 2012.

[43]. Blanchy, G., Saneiyan, S., Boyd, J., McLachlan, P. & Binley, A.; "ResIPy an Intuitive Open-Source Software for Complex Geoelectrical Inversion", Modeling, Lancaster, 2020.

[44]. Mostafaei, K., & Ramazi, H.; "Investigating the applicability of induced polarization method in ore modelling and drilling optimization: a case study from Abassabad, Iran," Near Surface Geophysics, vol. 17, no. 6-Recent Developments in Induced Polarization, pp. 637-652, 2019.